Dear Editor,

We thank for all the constructive comments and suggestions from referees. We have carefully addressed and provided detailed explanations for their concerns. Point-by-point responses to the suggestions, corresponding updates with the revised manuscript, and the finalized version have been uploaded.

In the following, original suggestions, our response, and updates on the revised manuscript are shown in **bold**, normal, and *italic*, respectively.

Kind Regards,

Jing Chen, Yuhang Hao, and Peizhao Li

Anonymous Referee #2

General comments:

The authors have addressed the comments and suggestions satisfactorily, which has raised some additional questions and clarifications, as noted below. These should be addressed before the manuscript is accepted for publication.

Response: Thanks for the comments and suggestions.

Specific comments:

RC1. It is now clear that the NPF frequencies in 2022 (heatwave) and 2023 (no heatwave) were identical. Furthermore, the NPF frequencies were similar between P1 and P2 in 2022 (study period). This indicates that NPF was not triggered or induced by the extremely hot conditions (heatwave) in 2022. The NPF start times in 2022 and 2023 are also comparable (±1 hour). If the mean NPF start time is calculated, it is likely to match closely. Therefore, the authors should modify the manuscript title accordingly, replacing "induced by heatwaves" with "during heatwaves" or "during extremely hot conditions in 2022." As a result, the nomenclature used is also not appropriate. I again suggest changing it to NPF polluted and NPF clean. HW

Response: We appreciate this suggestion. We have adjusted the title into "Divergent changes in aerosol optical hygroscopicity and new particle formation during heatwaves of summer 2022", as well as the nomenclatures into " $NPF_{polluted}$ " and " $NPF_{clean, HW}$ " throughout the manuscript/supplement including figures.

RC2. P2 refers to clean (HW) time period with lower PM_{2.5} (or aerosol scattering coefficient) which means that lower scavenging loss for smaller particles, however, I see that lower-size particles are consistently missing during this time period (Fig. 1i), while the banana starts from the lowest measured size during P1. How do you explain this? This is clearly obvious from the contour plot of PNSDs (Fig. 1i)

Response: We have confirmed the reliablity of field observations first by checking through the raw size distribution data. The reduced concentrations of nucleation mode particles during P2 are likely attributed to the influence of transport on the nucleation process during heatwaves (Cai et al., 2023; Lee et al., 2019). Namely, some nucleation mode particles were transported from upwind regions and had undergone atmospheric aging thereby a certain degree of growth upon arrival, resulting in relatively lower concentrations of smaller-sized particles than the case of locally formed. Such phenomena have also been documented in previous studies. For instance, some NPF events observed on Fukue Island exhibited particle growth without high concentrations of sub-5 nm particles, a possible explanation for which is that nucleation occurred upstream of the observation site, with newly formed particles growing to larger sizes during transport (Lee et al., 2019). Similarly, Cai et al. (2023) concluded that regional transport played a critical role during NPF events in the Lulang River valley, where the concentrations of 5-10 nm particles were consistently lower than those of 10-50 nm particles.

Here we selected two different NPF days to demonstrate the cumulative contributions of local growth and transportation to the number concentration of nucleation mode particles (Figure R1). The calculation methods for the contributions of local growth and transport factor were introduced in Cai et al. (2018). The nearly negative contribution of transportation implies that the NPF_{polluted} events in P1 were mainly driven by local growth (Figure R1a), while transportation had outweighted local growth as a key factor for P2 NPF_{clean}, HW days during heatwaves. Nevertheless, the comprehensive investigation of the mechanisms driving different NPF events, including the contribution of transportation to NPF, will be detailed in another work and is out the scope of this study. We have revised the manuscript as below to address the concern:

L358-363: The reduced $N_{Nuc.}$ during P2 period were likely attributed to the influence of transport on the local nucleation process (Fig. S4; Cai et al., 2023; Lee et al., 2019). Namely, some nucleation mode particles transported from upwind regions had undergone atmospheric aging thereby a certain degree of growth upon arrival (Cai et

al., 2023), resulting in relatively lower concentrations of smaller-sized particles than the case of locally formed.

Updates in the reference list:

Cai, R., Chandra, I., Yang, D., Yao, L., Fu, Y., Li, X., Lu, Y., Luo, L., Hao, J., Ma, Y., Wang, L., Zheng, J., Seto, T., and Jiang, J.: Estimating the influence of transport on aerosol size distributions during new particle formation events, Atmos. Chem. Phys., 18, 16587–16599, https://doi.org/10.5194/acp-18-16587-2018, 2018.

Lee, K., Chandra, I., Seto, T., Inomata, Y., Hayashi, M., Takami, A., Yoshino, A., and Otani, Y.: Aerial observation of atmospheric nanoparticles on Fukue Island, Japan, Aerosol Air Qual. Res., 19, 981–994, https://doi.org/10.4209/aaqr.2018.03.0077, 2019.

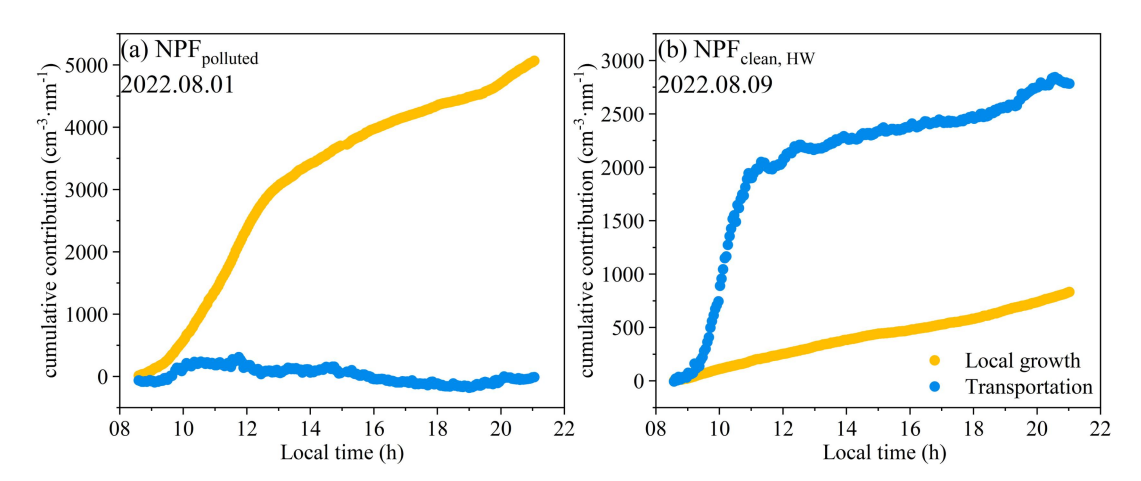


Figure R1. The cumulative contributions of transportation and local growth to the nucleation mode particle number concentration on a $NPF_{polluted}$ day (a) and a $NPF_{clean, HW}$ day (b) of this study.

RC3. The air mass history clearly shows that the origin of the air masses was the same across different event types. However, as the trajectories are overlaid, not all of them are clearly visible. The authors could examine the air mass history over three days and also consider the trajectory altitude to determine if there are any differences.

Response: Following the reviewer's suggestion, we have examined the 48-h and 72-h

air mass history back trajectories at 500 or 1000 m altitude above the site during the study period (Figure R1). The results consistently show that air masses during the study period predominantly originated from the southern region, regardless of event types. This homogeneity suggests that air mass origin was unlikely a primary driver of the observed differences in NPF event characteristics. We have replaced the original Figure S4b into the Figure R2.

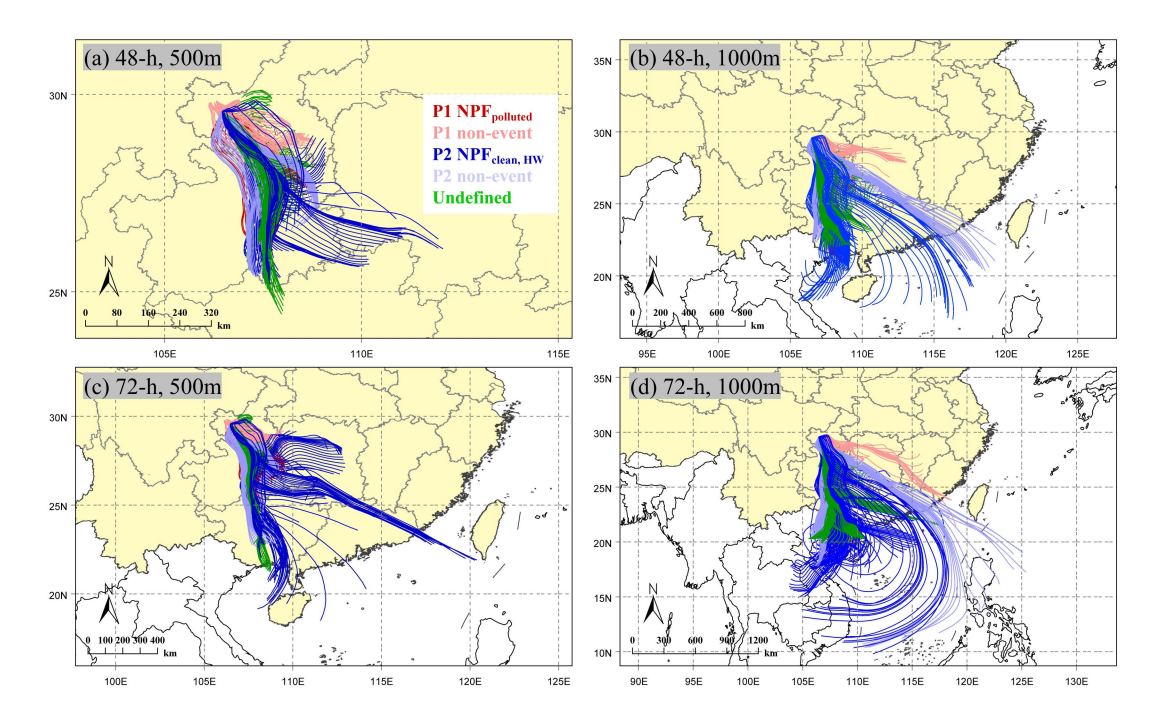


Figure R2. The 48-h and 72-h air-mass back trajectories at 500 or 1000 m altitude during the study period.

Updated on the Supplement:

L133-137: By using the HYSPLIT (Hybrid Single-Particle Lagrangian Integrated Trajectory) 4 model developed by NOAA (Stein et al., 2015), the 48-h and 72-h back trajectories of air masses at 500 or 1000 m altitude above the observation site during this study period were calculated and visualized by MeteoInfoMap (version 3.9.9; Figure S4b) (Chen et al., 2021; Tian et al., 2021; Wang, 2014).

RC4. The NPF frequencies in Fig. S4 differ from those presented in Fig. R2(a).

Response: Thank you for pointing out the inconsistency due to our carelessness.

Upon re-examining the original data, we identified a missing day of size distribution measurements during P1. This day was excluded as a null value in the revised analysis, but we forgot to update Fig. R2(a) in the initial response. We have now corrected it accordingly.

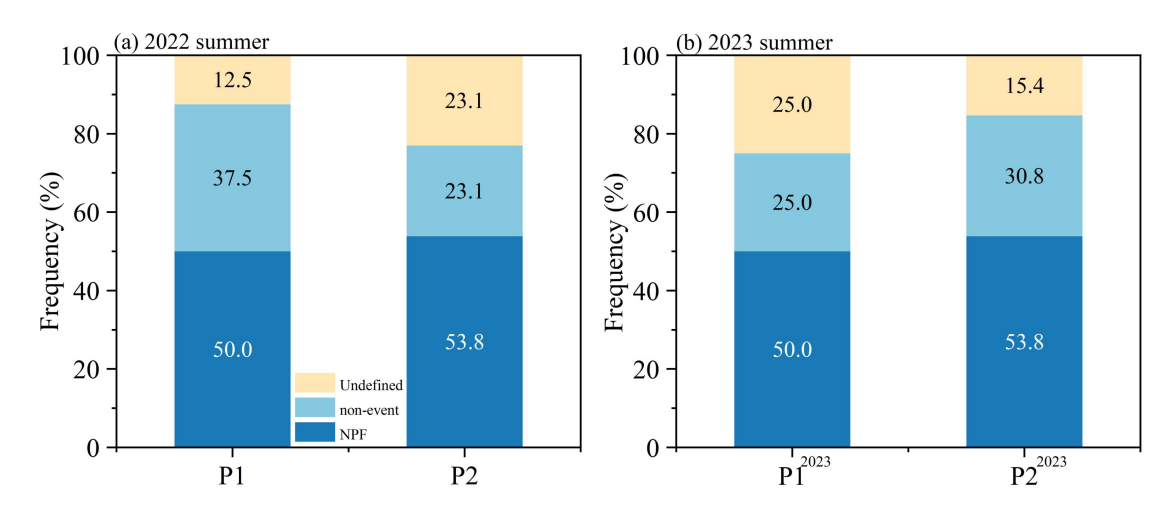


Figure R3. The occurrence frequencies of NPF, non-event and Undefined days during P1 ($P1^{2023}$) and P2 ($P2^{2023}$) periods of summer 2022 (2023).

RC5. What does NF_{ACC}, stand for? Does it refer to the number fraction of accumulation mode particles? Why focus on accumulation mode and number fractions? It would be more appropriate to first examine nucleation and Aitken mode particle number (absolute) concentrations, and then number fractions may be presented.

Response: Yes, the NF_{Acc.} (VF_{Acc.}) stands for the number (volume) fraction of accumulation mode particles in this study. According to reviewer's suggestion, we have displayed the number (volume) concentrations of different mode particles in Figure R4. Despite their lower number concentration compared to ultrafine particles, the accumulation mode particles contribute significantly to aerosol volume concentrations and light scattering (Figure R4, Figure S10a). Therefore, it is more appropriate to correlate NF_{Acc.} and VF_{Acc.} with the aerosol optical and hygroscopic properties (Figure 4).

We have revised the manuscript as follows:

L353-358: Distinct particle size distributions were observed for different NPF event

days. While the number concentrations of Aitken mode particles (N_{Ait}) were comparable during NPF days of both periods, the corresponding number concentration of nucleation mode (N_{Nuc}) was significantly higher on P1 NPF_{polluted} days (1880.8 \pm 2261.5 cm⁻³) than that for P2 NPF cases (1132.0 \pm 1333.5 cm⁻³) (Fig. 1i, Fig. S7).

L422-423: Given that NPF would largely enhance the abundance of both nucleation and Aitken mode aerosols (Fig. S7),

L469-472: Although ultrafine particles exhibited higher number concentrations during the study period, accumulation mode particles dominated the aerosol volume concentration and consequently contributed predominantly to the total light scattering (Figs. S7, S13).

L618-621: characterized with the smallest aerosol R_{eff} (102.8 \pm 12.4 nm) (Figure. S6), lowest number concentration (1897.0 \pm 680.8 cm⁻³) and fraction (0.20 \pm 0.10) of accumulation mode particles, intensified photooxidation, and a higher SOC/OC ratio.

Updated on the Supplement:

The Figure R4 has also been added into the Supplement (i.e., Figure S7):

L150-153: The PNSD is typically categorized into three modes: the nucleation mode $(D_p < 25 \text{ nm})$, Aitken mode (25-100 nm), and accumulation mode $(D_p > 100 \text{ nm})$ (Zhu et al., 2021). The number concentrations and volume concentrations of different mode particles for different event categories are shown in Figure S7.

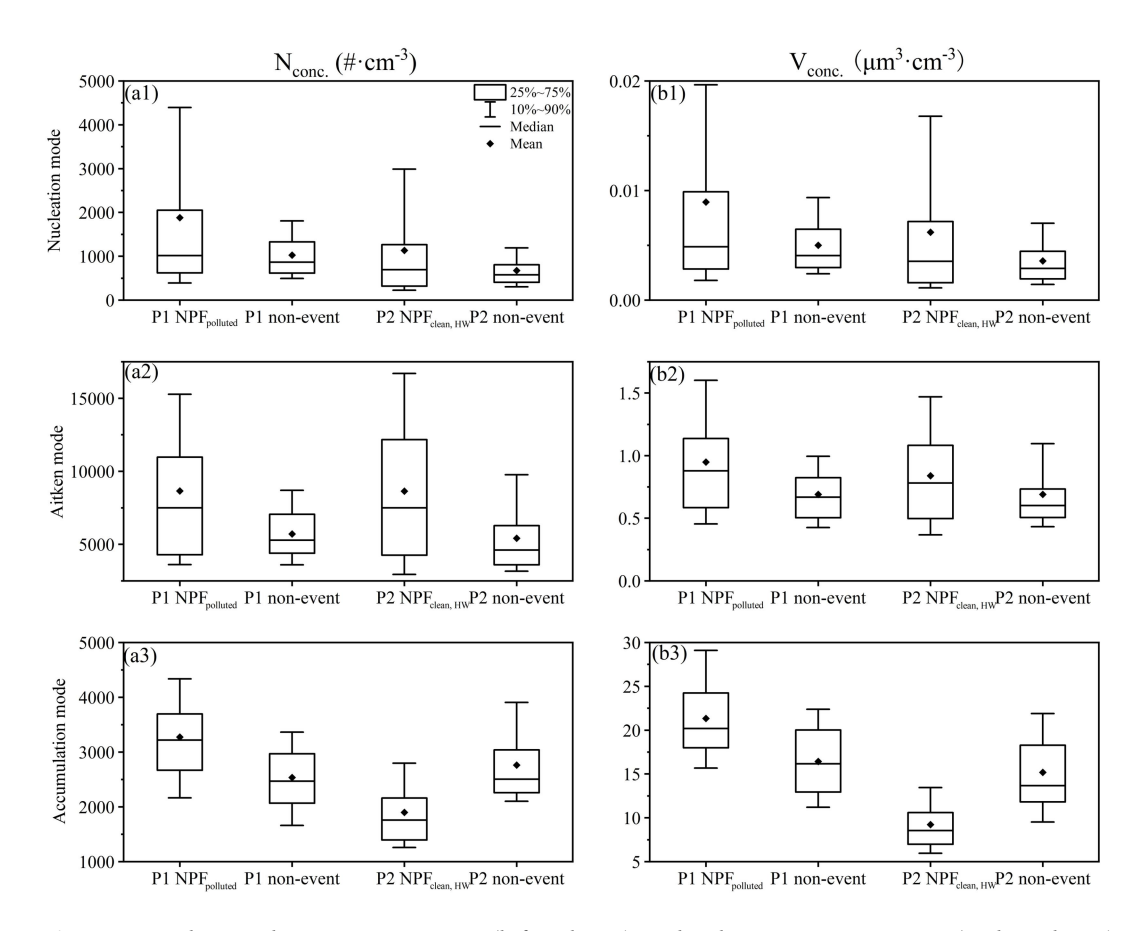


Figure R4. The number concentrations (left column) and volume concentrations (right column) of different mode particles for different event categories.

RC6. In Figs. 4 and 5, it is unclear how SAE and CS can be comparable. SAE is wavelength-dependent parameter and represents the total aerosol present in the atmosphere, whereas CS is calculated based on the measured size distribution within a specific size range (10–700 nm).

Response: We agree with this insightful comment. While our original intention was to highlight that higher SAE generally corresponded with lower scattering coefficients and cleaner conditions that is more favorable for NPF (lower CS), we acknowledge that SAE is not directly connected with CS. To avoid unnecessary misleading, we have removed the corresponding information of CS from Figure 5 and related discussions from the manuscript.

L506-510: Given that larger $\sigma_{sca, 525}$ values typically indicate the condition of a higher aerosol loading, f(RH) increased with SAE whereas decreased with $\sigma_{sca, 525}$, or rather the pollution level, during NPF days. The cleaner environment of P2 period may

further favor the occurrence of NPF event.

L701-703: A significantly positive (negative) correlation between f(RH) and SAE ($\sigma_{sca, 525}$, or rather the pollution level) was observed on NPF days for both periods, accompanied by higher f(RH) and SAE values on $NPF_{clean, HW}$ days.

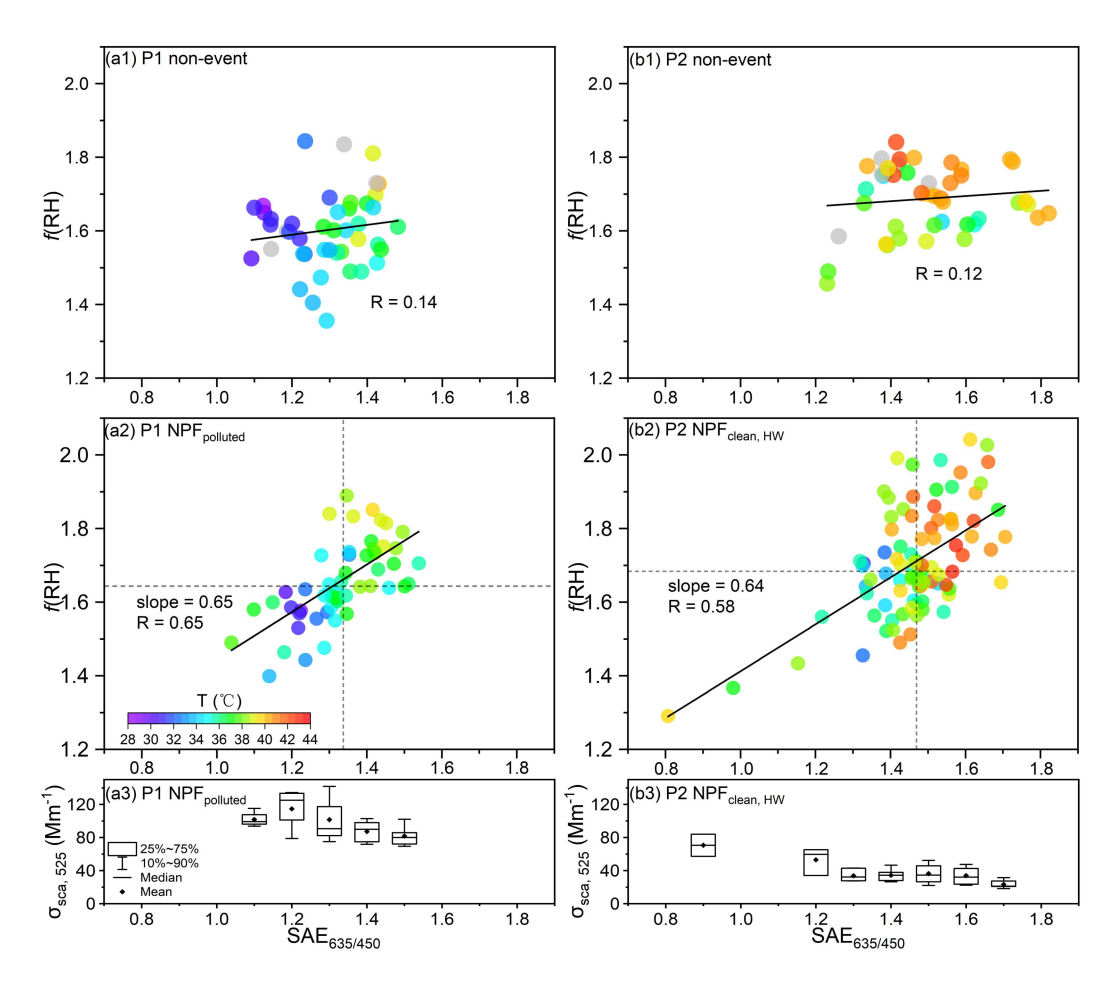


Figure 5. The relationship between f(RH) and $SAE_{635/450}$, as well as temperature (as indicated by the color of dots, missing values are represented in gray), on P1 non-event days (a1), NPF_{polluted} days (a2) during the 08:00-22:00 LT time window. The vertical (horizontal) dash line represents the median value of $SAE_{635/450}$ (f(RH)). (a3) The corresponding $\sigma_{sca, 525}$ under different $SAE_{635/450}$ levels on P1 NPF_{polluted} days. (b1-b3) The same but for P2 period.

RC7. What is the average FR and GR for P1 and P2? Are they similar, or different?

Response: We have added the mean FR and GR results into the Table S2 into the Supplement, and both FR and GR were generally lower for P2 NPF_{clean, HW} days. We

have also updated the corresponding results in the manuscript. Please kindly see Table S2 and our original response (RC6 of Referee #2).

Anonymous Referee #3

The authors have revised the manuscripts thoroughly. One major concern on the discrepancy observed in the ratio of HBF₅₂₅, RH/HBF₅₂₅ with previous studies was left.

Response: In our study, the cases of HBF_{525, RH}/HBF₅₂₅ >1 were generally observed under conditions of extremely low $\sigma_{sca, 525}$ and $\sigma_{bsca, 525}$ levels (Figure R5), particularly during NPF event days in the P2 heatwave period. This signifies that contributions of optically-insensitive ultrafine particles to $\sigma_{sca, 525}$ and especially to $\sigma_{bsca, 525}$ were amplified upon humidification, leading to significantly higher HBF of these hydrated fine particles thereby elevated HBF_{525, RH} levels (i.e., HBF_{525, RH}/HBF₅₂₅ >1).

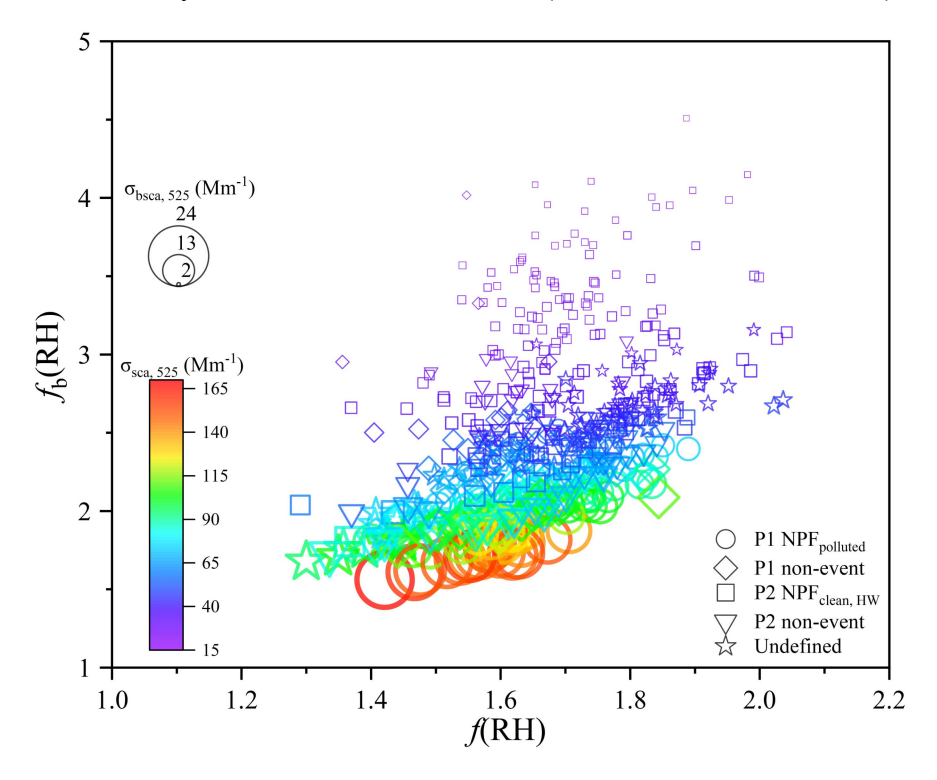


Figure R5. The relationship between f(RH), $f_b(RH)$, $\sigma_{sca, 525}$ (symbol color), $\sigma_{bsca, 525}$ (symbol size) in this study.

The higher HBF₅₂₅, RH/HBF₅₂₅ ratios observed in this study fundamentally reflect that the enhancement of aerosol backscattering coefficient (σ_{bsca}) upon hygroscopic growth can be stronger than that of the total light scattering (σ_{sca}) (Eq. 1). Namely, the $f_b(RH)$ (aerosol backscattering enhancement factor) was higher than f(RH).

$$HBF_{525, RH}/HBF_{525} = \frac{\sigma_{bsca525, RH}}{\sigma_{sca525, RH}} / \frac{\sigma_{bsca,525}}{\sigma_{sca,525}} = \frac{\sigma_{bsca525, RH}}{\sigma_{bsca,525}} / \frac{\sigma_{sca525, RH}}{\sigma_{sca,525}} = \frac{f_b(RH)/f(RH)}{f(RH)}$$
 (1)

While the observed HBF_{525, RH} ($f_b(RH)$) generally exceeding HBF₅₂₅ (f(RH)) seems to be different from previous studies (Titos et al. 2021; Xia et al. 2023), this phenomenon is actually not unprecedent (Figure R6). For instance, the higher HBF_{525, RH} (or higher $f_b(RH)$) could be found in Figure 2 of Fierz-Schmidhauser et al. (2010) and Figures 6-8 of Carrico et al. (2003) (Figure R6). As a matter of fact, this concern can be partly addressed theoretically with the Mie model.

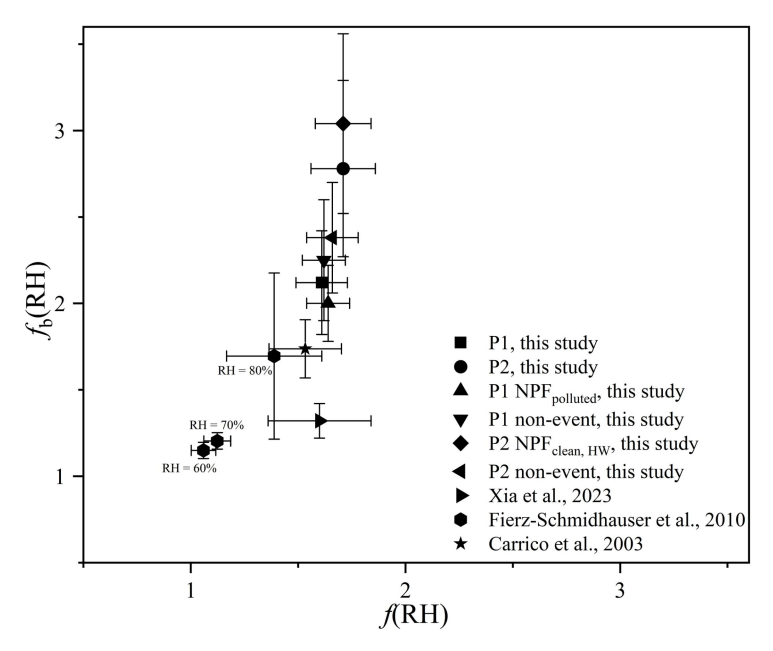


Figure R6. Scatterplot of $f_b(RH)$ versus f(RH) in this study (the mean levels for both P1 and P2 periods, and for different event categories), results from the study of Xia et al. (2023), Fierz-Schmidhauser et al. (2010) and Carrico et al. (2003). The error bars stand for the corresponding \pm one standard deviations.

Namely, the size-dependent efficiencies of light scattering (σ_{sca}), backscattering (σ_{bsca}) and hemispheric backscattering fraction (HBF= $\sigma_{bsca}/\sigma_{sca}$) in dry conditions, as well as the corresponding enhancements in these efficiencies of a single particle upon hydration (i.e., RH=85% for this study) at a specific visible wavelength (e.g., λ = 525 nm) could be simulated using the Mie model. It should be noted that the aerosol diameter growth factor, g(RH), was necessary for calculating aerosol optical properties due to the size growth after humidification (Brock et al., 2016; Tan et al.,

2024). g(RH) is normally determined by the aerosol hygroscopicity parameter κ , and the bulk aerosol $\kappa_{f(RH)}$ of this study was derived from the f(RH) measurements based on the method proposed by Kuang et al. (2017). According to the size distributions (Fig.S5) measured during the study period, the aerosol population was typically divided into the ultrafine ($D_p < 100$ nm; Uf.) and accumulation ($D_p \ge 100$ nm; Acc.) modes. Although the size-resolved κ results were unavailable, the mean κ_i for both ultrafine and accumulation mode particles could be roughly estimated assuming that $\kappa_{f(RH)}$ is a linear combination of volume-weighted κ_i for different modes (e.g., $\kappa_{f(RH)}$ = VF_{Uf.}* $\kappa_{Uf.}$ + VF_{Acc.}* $\kappa_{Acc.}$; Hong et al., 2024). Given a generally weaker hygroscopicity for the ultrafine mode (Chen et al., 2012; Petters and Kreidenweis, 2007), the mean κ of ultrafine particles was defined to be half of the measured bulk $\kappa_{f(RH)}$, and κ of accumulation mode particles can be derived from the bulk $\kappa_{f(RH)}$ with the corresponding volume fractions (i.e., VF_{Uf.} and VF_{Acc.}); consequently, the corresponding g(RH) for both Uf. and Acc. modes can be calculated with the κ -Köhler theory.

The complex refractive index is another critical input parameter for the Mie model, with the real part of complex refractive index (n) determining the aerosol light scattering ability. Under the assumption of a fixed n for dry aerosols ($n_{\rm dry} = 1.53$) in this study, the volume-weighted n of hydrated particles can be derived with $n_{\rm dry}$ and f(RH)-derived volume fractions of uptake water, f_W (Chen et al., 2012): $n = 1.33 * f_W + 1.53 * (1-f_W)$, where 1.33 is the n of pure water (Jung et al., 2016). Hence, the efficiencies of $\sigma_{\rm sca}$, $\sigma_{\rm bsca}$ and HBF after hygroscopic growth could be simulated with the time-averaged dry PNSD, the mean g(RH) of Uf. Mode (1.15) and Acc. mode (1.27), and the mean n of humidified aerosols (1.44) for the observation period. The theoretically calculated results were displayed in Figure R7.

Different from the significant ascending trend of σ_{sca} efficiencies within the size range of around 100~500 nm (Fig. R7a), the efficiency of σ_{bsca} (thereby HBF) presents a rather more periodic fluctuation with the particle size. This further leads to the pronounced variations in efficiencies of both σ_{bsca} and HBF upon hydration (Fig. R7b), and the enhancement of HBF_{525, RH} efficiency exhibited distinct size-dependent

sensitivity regimes. Namely, the efficiency ratio of HBF_{525, RH}/HBF₅₂₅ remained approximately 1 when D_p <100 nm, and the ratio gradually decreased below 1 with the particle size (in the range of 100~250 nm); however, it increased abruptly and largely exceeded 1 when D_P >250 nm, kind of with an oscillatory fluctuation. For instance, the efficiency of HBF_{525, RH}/HBF₅₂₅ could be above 24 (even reaching 30) when D_P was 289 nm (445 nm). Such a high level of HBF_{525, RH}/HBF₅₂₅ was actually observed in our study, with the sampled aerosol population contributed predominantly by particles smaller than 500 nm.

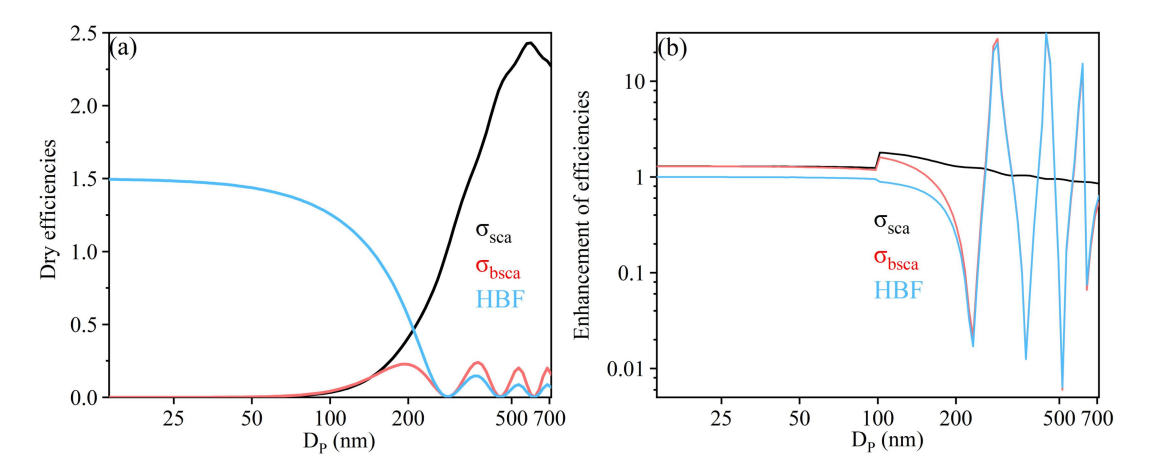


Figure R7. Size-dependent efficiencies of (a) light scattering (the black line), backscattering (the red line) and HBF (the blue line) in dry conditions, as well as (b) the enhancements in corresponding efficiencies of light scattering (the black line), backscattering (the red line) and HBF (the blue line) at $\lambda = 525$ nm simulated with the Mie theory.

To further investigate influences of the aerosol size distribution, hygroscopic properties, and composition-dependent complex refractive index on the HBF_{525, RH}/HBF₅₂₅ ratio, we conducted a sensitivity analysis with the measured data specifically for both P1 and P2 NPF days using the Mie model. Previous studies commonly assumed aerosol number size distributions as a combination of multi-lognormal distribution functions, with each mode representing a distinct particle population (Hussein et al., 2004):

$$\frac{dN}{d\log D_{P}} = \sum_{i=1}^{n} \frac{N_{t,i}}{\sqrt{2\pi} \log \sigma_{g,i}} \exp \left[-\frac{(\log D_{P} - \log \overline{D_{Pg,i}})^{2}}{2 \log^{2} \sigma_{g,i}} \right]$$
(2)

Where the three representative parameters, i.e., the total number concentration $N_{t,i}$, the geometric standard deviation (GSD) $\sigma_{g,i}$, and the geometrical mean diameter $D_{Pg,i}$, can be used to characterize an individual mode i; and n is the number of individual modes (Hussein et al., 2004). In this study, the measured PNSD data on NPF days during P1 and P2 periods were normally fitted into two modes: the predominant Uf. mode and the other one dominated by Acc. Mode particles. As a result, nine parameters were employed in the Mie model: four parameter pairs (D_{Pg} , GSD, N_t and g(RH)) for both Uf. and Acc. mode particles, along with the mean n of the bulk aerosol population upon hydration. Further, the HBF₅₂₅, RH/HBF₅₂₅ can be simplified as a function of aerosol size distribution (i.e., D_{Pg} , GSD, N_t), water uptake (e.g., g(RH)), and n as below:

HBF 525, RH/HBF 525 =
$$f(D_{Pg}, GSD, N_{t}, g(RH), n)$$
 (3)

The influence of a specific parameter on the HBF₅₂₅, RH/HBF₅₂₅ was evaluated by fixing all the other parameters at their measured mean values and computing HBF₅₂₅, RH/HBF₅₂₅ ratios across the range of this target parameter. For instance, the sensitivity of D_{Pg} could be illustrated as:

$$f(HBF_{525, RH}/HBF_{525}, D_{Pg}) = f(D_{Pg}, \overline{GSD}, \overline{N_t}, \overline{g(RH)}, \overline{n})$$
(4)

The measured mean value and variation range of each parameter were summarized in Table R1. The ranges of D_{Pg} , GSD, N_t and g(RH) were determined based on field measurements of this study. Zhao et al. (2021) reported that n of diverse aerosol populations could range from 1.36 to 1.78 across different Chinese cities, and this study constrained n to vary from 1.3 (nearly pure water of 1.33; Jung et al., 2016) to 1.8 (similar to black carbon of approximately 1.87; Schkolnik et al., 2007) in the modeling framework.

Table R1. A summary of the input parameters for the sensitivity analysis with the Mie models.

	Variable	Mode	Mean	Range
P1 NPF _{polluted}	D_{Pg} (nm)	Uf.	39	14-100
		Acc.	173	100-300
	GSD	Uf.	1.69	1.2-2.1

		Acc.	1.56	1.2-2.7
	M (43)	Uf.	16,844	2,000-28,000
	N_t (#·cm ⁻³)	Acc.	2,311	1,000-5,500
	g(RH)	Uf.	1.14	1.0-1.3
		Acc.	1.26	1.0-1.3
	n	/	1.45	1.3-1.8
P2 NPF clean, HW	D_{Pg} (nm)	Uf.	39	14-100
		Acc.	150	100-300
	GSD	Uf.	1.46	1.2-2.1
		Acc.	1.65	1.2-2.7
	N_t (#-cm-3)	Uf.	14,963	2,000-28,000
		Acc.	2,251	1,000-5,500
	g(RH)	Uf.	1.15	1.0-1.3
		Acc.	1.27	1.0-1.3
	n	/	1.44	1.3-1.8

The sensitivity tests revealed that the calculated HBF₅₂₅, RH/HBF₅₂₅ ratios commonly exceeded 1, with enhanced values for P2 NPF_{clean}, HW days (Figures R8-9), which is consistent with the observations. The influences of the PNSD and hygroscopicity related parameters (i.e., D_{Pg}, GSD, N_t and g(RH)) on HBF₅₂₅, RH/HBF₅₂₅ were displayed in Figure R8. Generally, the pattern of the PNSD (e.g., D_{Pg} and GSD) exhibited a much more significant impact on the HBF₅₂₅, RH/HBF₅₂₅ ratio than that of the total particle number concentration (N_t), the influence of which was almost negligible as indicated by the insignificant changes in the calculated HBF₅₂₅, RH/HBF₅₂₅ ratios. Particularly, the HBF₅₂₅, RH/HBF₅₂₅ ratio increased evidently with the mode diameter and GSD (e.g., HBF₅₂₅, RH/HBF₅₂₅ >1.5 at D_{Pg} = 200~300 nm and GSD >1.8) of the Acc. mode particles, specifically for smaller D_{Pg} and GSD (i.e., narrower distributions) of Uf. mode particles during NPF days (Figure R8a1-b2). However, HBF₅₂₅, RH/HBF₅₂₅ tends to be less sensitive to g(RH)

regardless of the aerosol mode, likely due to the predefined mode diameters and the smaller variation range of g(RH) used for the sensitivity tests (Table R1). Furthermore, HBF_{525, RH}/HBF₅₂₅ increased notably with n of hydrated particles, with a pronounced enhancement when n exceeded a threshold value (e.g., ~1.5) especially during P2 NPF days (Figure R8). The joint impacts of aerosol hygroscopic growth on HBF_{525, RH}/HBF₅₂₅ would depend on both the shift in the distribution pattern with the size growth and simultaneously lowered n due to enhanced liquid water content, highlighting the complex interactions of aerosol size distribution, water uptake, and optical properties in ambient atmospheric environment.

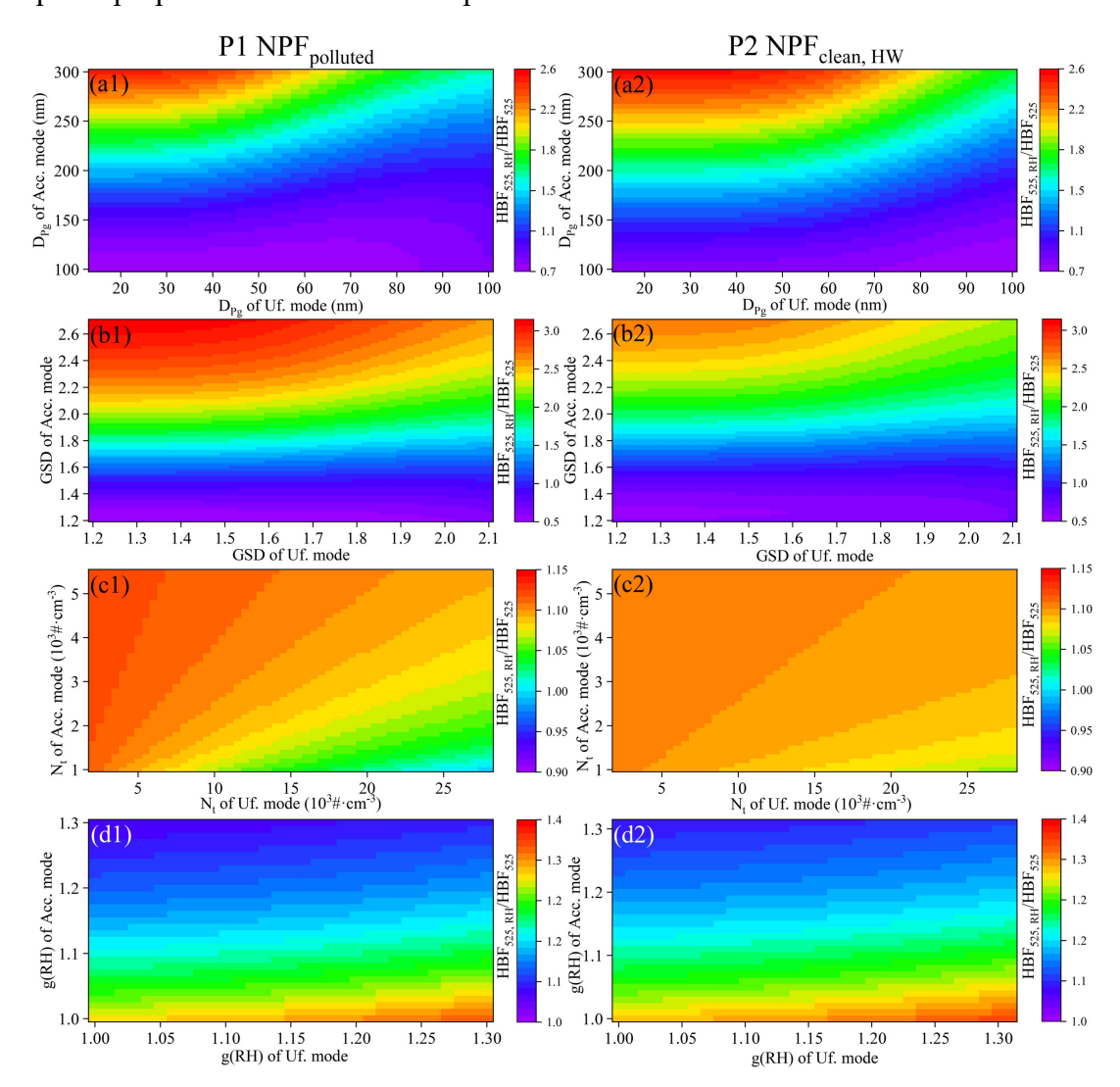


Figure R8. The relationships between the $HBF_{525, RH}/HBF_{525}$ ratios and the D_{pg} (a), GSD (b), N_t (c), g(RH) (d) of two modes particleas. The left (right) column was corresponding to the P1 $NPF_{polluted}$ (P2 $NPF_{clean, HW}$) days.

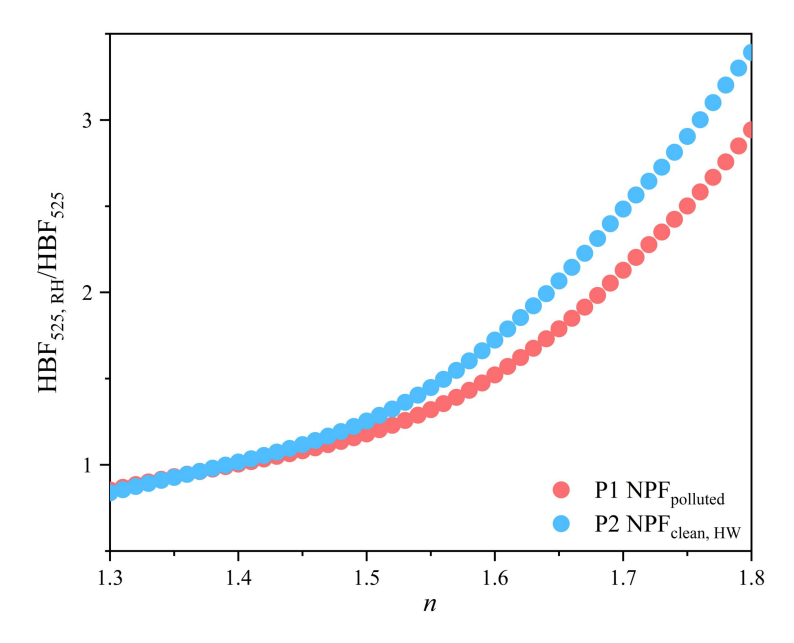


Figure R9. The variations of the $HBF_{525, RH}/HBF_{525}$ ratios with n levels on the different NPF days.

Another possible explanation could be related to the non-spherical particle morphology upon hygroscopic growth, which was hardly considered due to the precondition of spherical particles in the Mie model. Heterogeneous mixing of chemical components (e.g., secondary inorganics, organic coatings, as well as black carbon) can lead to the heterogeneity in particle bulk hygroscopicity (Yuan and Zhao, 2023), which may further affect the morphology of humidified particles. The more hydrophilic compositions would tend to be more spherical, otherwise with irregular shapes (Giordano et al., 2015; Tan et al., 2020; Tritscher et al., 2011). Furthermore, potential heterogeneity in the humidification process across the "wet" nephelometer chamber may have caused particles to partly exist in a semi-solid phase state (Tang et al., 2019). This combination of heterogeneity in aerosol hygroscopicity and hydration processes likely contributed to the non-spherical particle morphology even after humidification.

In summary, the observed elevated HBF₅₂₅, RH/HBF₅₂₅ ratios in this study can be attributed to the following aspects. Firstly, it could be related to the shift of aerosol size distribution toward larger accumulation-mode sizes (e.g., more sensitive to the enhancement in HBF) during the subsequent growth of both pre-existing and newly formed particles or upon hydration in the "wet" nephelometer. Additionally, the dominance of organic components during the study period likely introduced

heterogeneity in aerosol hygroscopicity, which may alter particle morphology upon water uptake. Moreover, aerosol n tends to increase with the aging process of organic components (Moise et al., 2015; Zhao et al., 2021), suggesting that particles may have higher n values during P2 period with the higher photooxidation intensity, thereby contributing to the observed enhancement in the HBF_{525, RH}/HBF₅₂₅ ratio.

We have updated the manuscript as follows:

L582-591: Additionally, the predominant organic components when heterogeneously mixed with diverse chemical compositions (e.g., inorganics and black carbon) likely introduced the heterogeneity in aerosol hygroscopicity (Yuan and Zhao, 2023), which may alter particle morphology thereby optical properties upon water uptake (Giordano et al., 2015; Tan et al., 2020; Tritscher et al., 2011). The efficient evaporation of organic coatings under extremely hot conditions could also contribute to the change in particle morphology (e.g., non-spherical inregular shapes) upon humidification, as evidenced by a recent study that high temperature conditions could accelerate the evaporation rate of SOA (Li et al., 2019).

L599-621: Another possible reason is the distinct size dependences of both light scattering and backscattering efficiencies (Fig. S11a), with much more significant enhancements in the backscattering efficiency thereby HBF specifically of accumulation mode particles after hygroscopic growth (Fig. S11b). As reflected by the Mie model, although the abundant newly formed particles were generally optically-insensitive (e.g., below 100 nm), their contributions to σ_{sca, 525} and especially to σ_{bsca, 525} could be amplified upon humidification (Fig. S11b). Besides, the shift of size distribution towards larger accumulation-mode particles could also result in a significant elevation in HBF_{525, RH}/HBF₅₂₅ ratios, especially under the condition of a smaller mode diameter and narrower distribution of ultrafine-mode particles (e.g., during NPF events) (Fig. S15a1-b2 for the theoretical sensitivity tests of Sect. S9 in the supplement). Furthermore, the HBF_{525, RH}/HBF₅₂₅ ratio exhibited a significant positive correlation with the real part of complex refractive index (n) of bulk aerosols (Fig. S16), and n tends to increase with the aging process of organic species (Moise et al., 2015; Zhao et al., 2021). In this sense, the evolution of both aerosol size

distribution pattern and chemical compositions, combined with the heterogeneity in aerosol hygroscopicty, could potentially change particle morphology and optical properties (e.g., complex refractive index and elevated HBF_{525, RH}) particularly during heatwave-influenced NPF_{clean, HW} days, characterized with the smallest aerosol $R_{\rm eff}$ (102.8 \pm 12.4 nm) (Figure. S6), lowest number concentration (1897.0 \pm 680.8 cm⁻³) and fraction (0.20 \pm 0.10) of accumulation mode particles, intensified photooxidation, and a higher SOC/OC ratio.

Updates in the reference list:

Giordano, M., Espinoza, C., and Asa-Awuku, A.: Experimentally measured morphology of biomass burning aerosol and its impacts on CCN ability, Atmos. Chem. Phys., 15, 1807–1821, https://doi.org/10.5194/acp-15-1807-2015, 2015.

Moise, T., Flores, J. M., and Rudich, Y.: Optical Properties of Secondary Organic Aerosols and Their Changes by Chemical Processes, Chem. Rev., 115, 4400–4439, https://doi.org/10.1021/cr5005259, 2015.

Tritscher, T., Jurnyi, Z., Martin, M., Chirico, R., Gysel, M., Heringa, M. F., Decarlo, P. F., Sierau, B., Prévt, A. S. H., Weingartner, E., and Baltensperger, U.: Changes of hygroscopicity and morphology during ageing of diesel soot, Environ. Res. Lett., 6, https://doi.org/10.1088/1748-9326/6/3/034026, 2011.

Yuan, L. and Zhao, C.: Quantifying particle-To-particle heterogeneity in aerosol hygroscopicity, Atmos. Chem. Phys., 23, 3195–3205, https://doi.org/10.5194/acp-23-3195-2023, 2023.

Zhao, G., Hu, M., Fang, X., Tan, T., Xiao, Y., Du, Z., Zheng, J., Shang, D., Wu, Z., Guo, S., and Zhao, C.: Larger than expected variation range in the real part of the refractive index for ambient aerosols in China, Sci. Total Environ., 779, 146443, https://doi.org/10.1016/j.scitotenv.2021.146443, 2021.

We have added the detailed Mie scattering simulations in S7 and replaced the original Figure S11a into the Figure R7, the sensitivity analysis and results have been added in S9, Figures S15-16 and Table S3 in Supplement.

Updates in the reference list of Supplement:

Brock, C. A., Wagner, N. L., Anderson, B. E., Attwood, A. R., Beyersdorf, A., Campuzano-Jost, P., Carlton, A. G., Day, D. A., Diskin, G. S., Gordon, T. D., Jimenez, J. L., Lack, D. A., Liao, J., Markovic, M. Z., Middlebrook, A. M., Ng, N. L., Perring, A. E., Richardson, M. S., Schwarz, J. P., Washenfelder, R. A., Welti, A., Xu, L., Ziemba, L. D., and Murphy, D. M.: Aerosol optical properties in the southeastern United States in summer - Part 1: Hygroscopic growth, Atmos. Chem. Phys., 16, 4987–5007, https://doi.org/10.5194/acp-16-4987-2016, 2016.

Chen, J., Zhao, C. S., Ma, N., Liu, P. F., Göbel, T., Hallbauer, E., Deng, Z. Z., Ran, L., Xu, W. Y., Liang, Z., Liu, H. J., Yan, P., Zhou, X. J., and Wiedensohler, A.: A parameterization of low visibilities for hazy days in the North China Plain, Atmos. Chem. Phys., 12, 4935–4950, https://doi.org/10.5194/acp-12-4935-2012, 2012.

Hong, J., Ma, J., Ma, N., Shi, J., Xu, W., Zhang, G., Zhu, S., Zhang, S., Tang, M., Pan, X., Xie, L., Li, G., Kuhn, U., Yan, C., Qi, X., Zha, Q., Nie, W., Tao, J., He, Y., Zhou, Y., Sun, Y., Xu, H., Liu, L., Cai, R., Zhou, G., Kuang, Y., Yuan, B., Wang, Q., Petäjä, T., Kerminen, V. M., Kulmala, M., Cheng, Y., and Su, H.: Low Hygroscopicity of Newly Formed Particles on the North China Plain and Its Implications for Nanoparticle Growth, Geophys. Res. Lett., 51, https://doi.org/10.1029/2023GL107516, 2024.

Hussein, T., Puustinen, A., Aalto, P. P., Mäkelä, J. M., Hämeri, K., and Kulmala, M.: Urban aerosol number size distributions, Atmos. Chem. Phys., 4, 391–411, https://doi.org/10.5194/acp-4-391-2004, 2004.

Jung, C. H., Shin, H. J., Lee, J. Y., and Kim, Y. P.: Sensitivity and contribution of organic aerosols to aerosol optical properties based on their refractive index and hygroscopicity, Atmosphere (Basel)., 7, https://doi.org/10.3390/atmos7050065, 2016.

Moise, T., Flores, J. M., and Rudich, Y.: Optical Properties of Secondary Organic Aerosols and Their Changes by Chemical Processes, Chem. Rev., 115, 4400–4439, https://doi.org/10.1021/cr5005259, 2015.

Schkolnik, G., Chand, D., Hoffer, A., Andreae, M. O., Erlick, C., Swietlicki, E., and Rudich, Y.: Constraining the density and complex refractive index of elemental and organic carbon in biomass burning aerosol using optical and chemical measurements, Atmos. Environ., 41, 1107–1118, https://doi.org/10.1016/j.atmosenv.2006.09.035, 2007.

Tan, F., Zhang, H., Xia, K., Jing, B., Li, X., Tong, S., and Ge, M.: Hygroscopic behavior and aerosol chemistry of atmospheric particles containing organic acids and inorganic salts, npj Clim. Atmos. Sci., 7, 1–21, https://doi.org/10.1038/s41612-024-00752-9, 2024.

Zhao, G., Hu, M., Fang, X., Tan, T., Xiao, Y., Du, Z., Zheng, J., Shang, D., Wu, Z., Guo, S., and Zhao, C.: Larger than expected variation range in the real part of the refractive index for ambient aerosols in China, Sci. Total Environ., 779, 146443, https://doi.org/10.1016/j.scitotenv.2021.146443, 2021.

References

- Carrico, C. M., Kus, P., Rood, M. J., Quinn, P. K., & Bates, T. S. (2003). Mixtures of pollution, dust, sea salt, and volcanic aerosol during ACE-Asia: Radiative properties as a function of relative humidity. *Journal of Geophysical Research:*Atmospheres, 108(D23). https://doi.org/10.1029/2003jd003405
- Fierz-Schmidhauser, R., Zieger, P., Gysel, M., Kammermann, L., DeCarlo, P. F., Baltensperger, U., & Weingartner, E. (2010). Measured and predicted aerosol light scattering enhancement factors at the high alpine site Jungfraujoch. *Atmospheric Chemistry and Physics*, 10(5), 2319–2333. https://doi.org/10.5194/acp-10-2319-2010